

# Something something something physics

Steven Green  
of Emmanuel College

A dissertation submitted to the University of Cambridge  
for the degree of Doctor of Philosophy



## Abstract

This thesis describes the optimisation of the calorimeter design for collider experiments at the future Compact Linear Collider (CLIC) and the International Linear Collider (ILC). The detector design of these experiments is built around high-granularity Particle Flow Calorimetry that, in contrast to traditional calorimetry, uses the energy measurements for charged particles from the tracking detectors. This can only be realised if calorimetric energy deposits from charged particles can be separated from those of neutral particles. This is made possible with fine granularity calorimeters and sophisticated pattern recognition software, which is provided by the PandoraPFA algorithm. This thesis presents results on Particle Flow calorimetry performance for a number of detector configurations. To obtain these results a new calibration procedure was developed and applied to the detector simulation and reconstruction to ensure optimal performance was achieved for each detector configuration considered.

This thesis also describes the development of a software compensation technique that vastly improves the intrinsic energy resolution of a Particle Flow Calorimetry detector. This technique is implemented within the PandoraPFA framework and demonstrates the gains that can be made by fully exploiting the information provided by the fine granularity calorimeters envisaged at a future linear collider.

A study of the sensitivity of the CLIC experiment to anomalous gauge couplings that effect vector boson scattering processes is presented. These anomalous couplings provide insight into possible beyond standard model physics. This study, which utilises the excellent jet energy resolution from Particle Flow Calorimetry, was performed at centre-of-mass energies of 1.4 TeV and 3 TeV with integrated lumi-

nosities of  $1.5\text{ab}^{-1}$  and  $2\text{ab}^{-1}$  respectively. The precision achievable at CLIC is shown to be approximately one to two orders of magnitude better than that currently offered by the LHC.

Finally, a study into various technology options for the CLIC vertex detector is described.

## Declaration

This dissertation is the result of my own work, except where explicit reference is made to the work of others, and has not been submitted for another qualification to this or any other university. This dissertation does not exceed the word limit for the respective Degree Committee.

Andy Buckley



## Acknowledgements

Of the many people who deserve thanks, some are particularly prominent, such as my supervisor...





## Preface

This thesis describes my research on various aspects of the LHCb particle physics program, centred around the LHCb detector and LHC accelerator at CERN in Geneva.

For this example, I'll just mention Chapter ?? and Chapter ??.



# Contents

<b>1 Particle Flow Calorimetry and Linear Collider Detectors</b>	<b>1</b>
1.1 Particle Flow Calorimetry . . . . .	1
1.2 Linear Collider Detectors . . . . .	3
1.2.1 Tracking System . . . . .	4
1.2.2 Electromagnetic Calorimeter . . . . .	7
1.2.3 Hadronic Calorimeter . . . . .	9
1.2.4 Forward Calorimetry . . . . .	10
1.2.5 Muon Chamber . . . . .	11
1.2.6 CLIC ILD . . . . .	12
1.3 PandoraPFA . . . . .	13
<b>Bibliography</b>	<b>21</b>
<b>List of figures</b>	<b>23</b>
<b>List of tables</b>	<b>25</b>



*“Writing in English is the most ingenious torture  
ever devised for sins committed in previous lives.”*

— James Joyce



# Chapter 1

## Particle Flow Calorimetry and Linear Collider Detectors

*“I am fond of pigs. Dogs look up to us. Cats look down on us. Pigs treat us as equals.”*

— Winston Churchill

### 1.1 Particle Flow Calorimetry

The premise of particle flow calorimetry is to use the sub-detector that offers the best energy resolution to measure the energy of any given particle. The biggest contrast to tradition calorimetry at particle collider experiments when using this approach is that the energy of charged particles are measured using the curvature of the path they transverse instead of measuring their energy using the calorimeters. In traditional calorimetry charged particle energies are measured predominantly in the HCal, while in particle flow calorimetry they are measured using the tracker. The tracker energy resolution for a single charged particle of energy  $E_{X^\pm}$  is  $\sim 10^{-4} \times E_{X^\pm}^2$ , while for the HCal it is  $0.55 \times \sqrt{E_{X^\pm}}$ . The energy resolution offered by the tracker is significantly better than that offered by the HCal for energies up to  $\sim \mathcal{O}(300)$  GeV and this is the origin of the improved performance offered by particle flow calorimetry. Particle flow calorimetry offers gains in performance for collision energies well beyond 300 GeV as the average long-lived particle energy for events of interest is typically much less than 300 GeV. The application of particle flow also leads to a significant improvement in the

measurement of jet energies as, after the decay of short-lived particles, approximately 60% of the energy of a jet is carried in the form of charged particles. The measurement of jet energy in the particle flow paradigm is summarised in table 1.1. The benefits to the energy resolution for both charged particles and jet offered by the particle flow approach to calorimetry is the driving factor behind why it will be used at the linear collider experiment. The jet energy resolutions will be invaluable for characterising multi-jet final states in physics processes of interest. Furthermore, the improved energy resolutions will be highly beneficial for quantifying those final states of interest that involving charged leptons and missing momentum.

Jet Component	Detector	Energy Fraction	Energy Resolution
Charged Particles ( $X^\pm$ )	Tracker	$\sim 0.6E_j$	$10^{-4} \times E_{X^\pm}^2$
Photons ( $\gamma$ )	ECal	$\sim 0.3E_j$	$0.15 \times \sqrt{E_\gamma}$
Neutral Hadrons ( $X^0$ )	HCal	$\sim 0.1E_j$	$0.55 \times \sqrt{E_{X^0}}$

**Table 1.1:** The approximate jet fractions and energy resolutions for charged particles ( $X^\pm$ ), photons ( $\gamma$ ) and neutral hadrons ( $X^0$ ). Taken from [6].

Particle flow calorimetry is challenging to put into practice as it requires a precise reconstruction for all long-lived particles within a detector. Charged particle energy measurements are made using the curvature of the track they transverse as they bend in the magnetic field, but they also produce calorimetric energy deposits, as shown in figure 1.1. If both energy measurements are included the energy of the charged particle will be double counted. To avoid this, any calorimetric energy deposits associated to charged particle tracks are not used when reporting the reconstructed energy. However, this means that if the calorimetric energy deposits for a neutral particle are incorrectly associated to a track, the energy measurement for that neutral particle will be totally omitted. The combination of this double counting of charged particle energies and loss of neutral particle energies form the confusion contribution to the jet energy resolution, which acts to degrade the energy resolution in the particle flow paradigm. Particle flow calorimetry hinges on the event reconstruction being able to correctly all charged particle tracks to their corresponding calorimetric energy



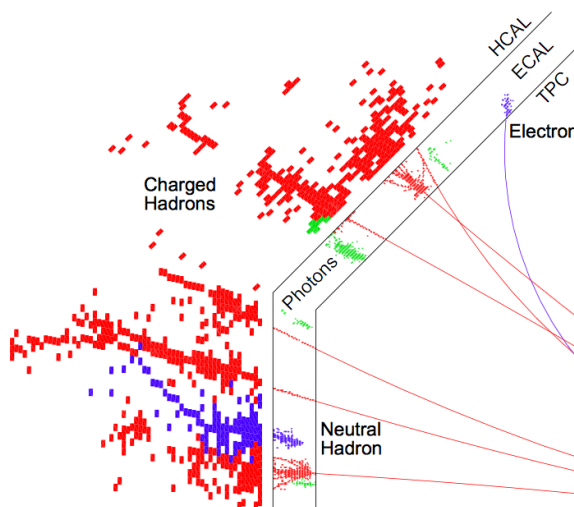


**Figure 1.1:** A typical simulated 250 GeV jet in the CLIC\_ILD detector, with labels identifying constituent particles. Image taken from [5].

deposits. This can only be realised by using calorimeters with fine segmentation so that it is possible to resolve individual particle showers within them coupled with sophisticated pattern recognition algorithms to reduce the effects of confusion.

## 1.2 Linear Collider Detectors

All detector concepts for the linear collider have been purposely built to make particle flow calorimetry possible. While there are a number of different concepts that are under consideration for both the ILC and CLIC one of the most prominent, and the focus of this work, is the International Large Detector (ILD). The ILD detector, shown in figure 1.2 realises very high spatial resolution for all sub-detector systems thanks to its highly granular calorimeters and central tracking system, all of which is encompassed within a 3.5 T magnetic field. When combined with sophisticated pattern recognition software provided by PandoraPFA, particle flow calorimetry can be realised and the jet energy resolution can reach the goal of 3.8% which is required to allow separation of hadronic decays from W and Z bosons. Details on each of the various sub-detector systems for ILD will now be discussed.

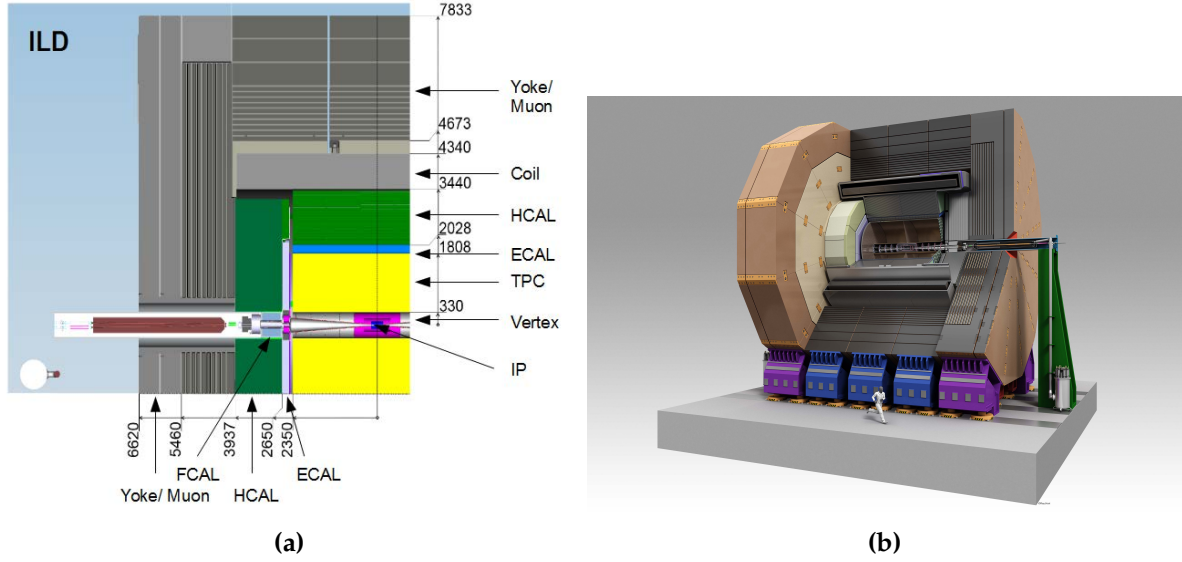


**Figure 1.2:** (a) Quadrant view of the ILD detector concept. The interaction point is in the lower right corner of the picture. Dimensions are in mm. (b) View of the ILD detector concept. Figures taken from [2].

### 1.2.1 Tracking System

The tracking system for the ILD detector consist of a multi-layer pixel-vertex detector, which is surrounded by a system of silicon strip and pixel detectors. These are purposed to give precise information about displaced vertices with respect to the impact point, which are crucial for the study of short lived particles such as the  $D$  or  $B$  mesons. Outside of the vertex detector the central tracker of ILD, which is a Time Projection Chamber (TPC). The TPC allows each charged particle track to be sampled at many space points giving precise information that can be used to extract the curvature of the track and the momentum of the charged particle transversing the track. Finally, a further silicon strip detector surrounds the TPC to give an additional, high precision, space point to aid in the tracking performance.

#### Vertex System

The main goal of the ILD vertex detector is to achieve a resolution on the impact parameter of charged particle tracks of  $\sigma_b < 5 \oplus \frac{10}{p \sin(\theta)^{3/2}} \mu\text{m}$ , where the first term is the transverse impact parameters resolution and the second is a multiple-scattering term. This makes it possible to precisely tag secondary vertices from charm and

bottom mesons, which typically have relatively short proper lifetimes,  $\tau$ , such that  $c\tau \approx \mathcal{O}(100 - 500)\mu\text{m}$ . To achieve this impact parameter resolution a spatial resolution of better than  $3\mu\text{m}$  is required near the IP will be required. Furthermore, a low material budget of less than  $0.15\% X_0$  per layer is needed to ensure that little energy is lost and that few electromagnetic showers are initiated within the tracker. A low pixel occupancy will be essential for determining the trajectory of individual tracks in the detector. The detector will have to be radiation hard to cope with the intense conditions found close to the IP due to the beam induced background, predominantly beamstrahlung. Furthermore, consideration will have to be given as to the mechanical structure of the detector, power consumption and cooling.

There are a number of different pixel technology options under consideration for the vertex detector for the ILD detector and this is an active area of ongoing research and development for the linear collider collaboration. The current design of the vertex detector consists of three concentric layers of double-sided ladders that are close to being cylindrical. Each ladder has two pixel sensors on each side and the ladder thickness is approximately 2 mm. The inner most radii of the ladders ranges from 16 mm to 60mm from the IP. In the simulation of the vertex detector silicon is used as the sensitive material and both support material and a cryostat is included for realism.

### Silicon Tracking System

There are four components that make up the silicon tracking system for ILD, shown in figure 1.3. These are the:

- Silicon Inner Tracker (SIT) and Silicon External Tracker (SET). These are both barrel components, which are positioned immediately inside and outside the TPC. They act to provide additional space points that can be used in track fitting. In particular these help to link the vertex detector with the TPC and help with extrapolation of TPC tracks into the calorimeter. These silicon sensors will have a  $50\mu\text{m}$  pitch and will contain  $200\text{ m}\mu$  thick silicon.
- Endplate of the TPC (ETD). This sensor is identical to the SET, but is positioned in front of the ECal endcap calorimeter to extend the coverage of this silicon envelope.
- Forward tracker (FTD). This detector consists of seven silicon disks, which extends the coverage of the tracking down to small angles which the TPC does not cover.

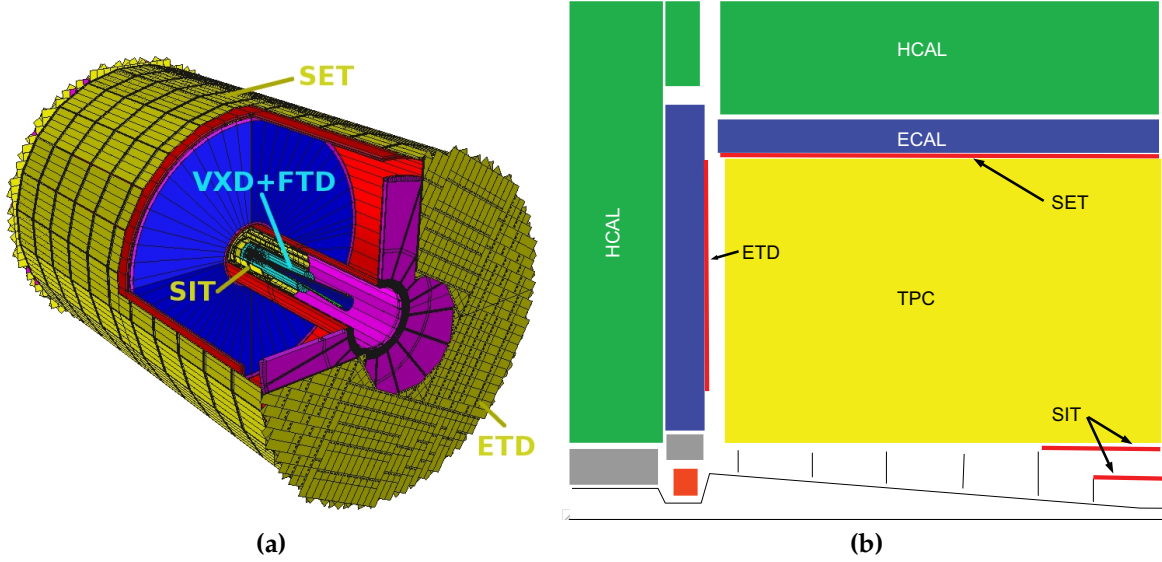


**Figure 1.3:** (a) A quadrant view of the ILD silicon envelope made of the four components SIT, SET, ETD and FTD as included in the full MOKKA simulation. (b) a 3D detailed GEANT4 simulation description of the silicon system. Figures taken from [2].

The requirements for these sensors is similar to those of the vertex detector in terms of requiring low material budget and low occupancy, however, as the sensors are further away from the IP radiation hardness is less crucial. The technology options for these sensors is also under development as was the case for the vertex detector. In the detector model simulations all of these elements are included with additional material added to represent the support structure.

## TPC

The central tracking system for the ILD detector is a TPC, which is shown in figure 1.4. The TPC consists of two chambers of gas that has a high voltage applies across it. Charged particles passing through the TPC ionise the gas and the ionised molecules drift in the high voltage to the end plates where they are collected and measured. The drift time is then used to calculate the position of the ionisation point. TPCs have the advantage over silicon tracking as they continuously track any charged particle passing through them unlike silicon detectors, which are only sensitive within the silicon layer. This compensates for the worse single point resolution that TPCs have in comparison to a silicon detectors and makes TPCs a viable option for the ILD detector. Furthermore, the TPC has a very low material budget, which benefits calorimetry in

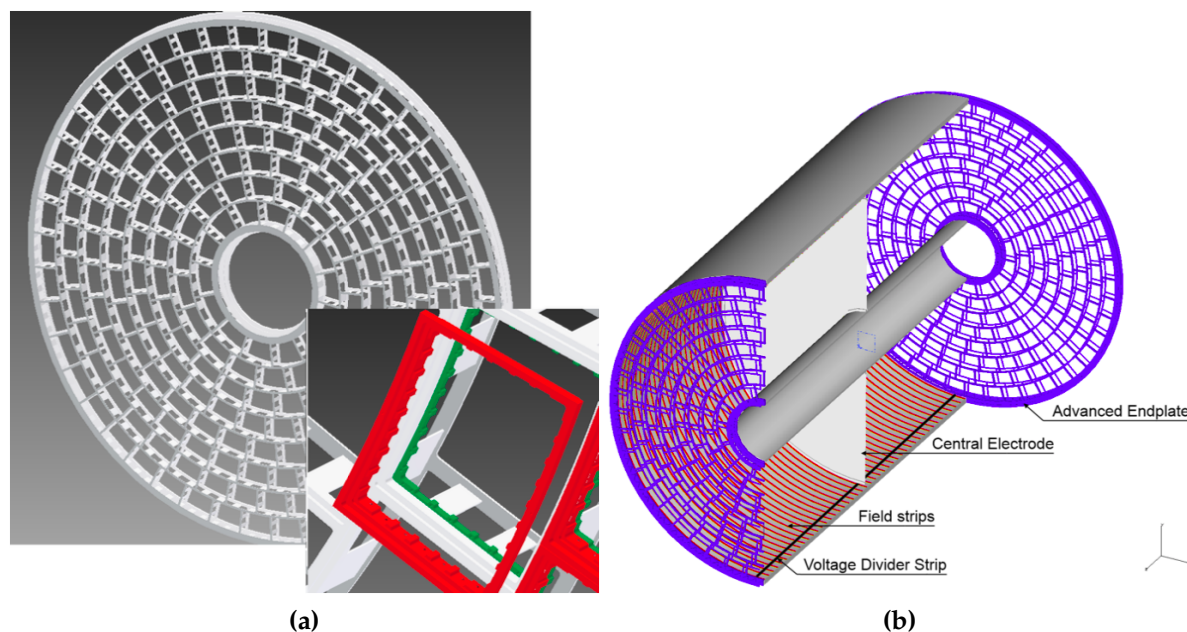


**Figure 1.4:** (a) Drawing of the proposed end-plate for the TPC. (b) Conceptual sketch of the TPC system showing the main parts of the TPC (not to scale). Figures taken from [2].

ILD. The TPC will operate within a 3.5 T magnetic field and under these conditions a point resolution of better than  $100 \mu\text{m}$  and a double hit resolution in  $\phi$  of less than 2 mm can be achieved. Several readout technology options that are dependent upon the gas mixture used for the TPC are currently under development. For all potential options it is envisaged that the readout pads would be  $\approx 1 \times 6\text{mm}^2$  giving a total of approximately  $10^6$  on the TPC endplates.

In the detector simulation the TPC is simulated as a cylindrical volume of the gas mixture,  $\text{Ar}:\text{CH}_4:\text{CO}_2$  (95:3:2) [1], which is surrounded by a realistic field cage. Furthermore, a conservative estimate of the endplate is included in the simulation, which accounts for the support structure, electronics and cooling pipes. Estimations have also been made for the material budget for power and readout cables that will serve the inner tracking detector. These are included in the simulation as an aluminium cylinder between the beam pipe and the field cage of the TPC.

### 1.2.2 Electromagnetic Calorimeter

A highly segmented electromagnetic sampling calorimeter (ECal) surrounds the ILD tracking system, which has been designed with particle flow calorimetry in mind. To

that extend the spatial resolution of particle showers within the ECal takes as much, if not more, precedence than the energy resolution. The nominal ILD ECal is a silicon tungsten sampling calorimeter, which contains 30 layers and uses square cells with side length 5 mm, however, a scintillator strip option is also being considered.

The primary goal of the ECal is to induce electromagnetic particles to shower within it and to record the energy deposited by those showers. To that extent the ECal is constructed using tungsten as the absorber material. As well as containing a large number of radiation lengths ( $X_0$ ) per unit length, see table 1.2, tungsten also has a small Molière radius and a large ratio of the radiation length to the nuclear interaction length. The small Molière radius will lead to compact electromagnetic showers and make the separation of nearby showers easier, while the large ratio of the radiation length to nuclear interaction length will lead to greater longitudinal separation between electromagnetic and hadronic showers. The use of tungsten in the nominal ILD ECal allows for a large number of radiation lengths,  $\approx 24X_0$ , to be compacted within a relatively short distance,  $\approx 20$  cm, which is sufficient for containing all but the highest energy electromagnetic showers. The compact nature of the ECal also helps to reduce the overall size and cost of the detector. A good energy resolution can be achieved with this configuration if 30 sampling layers are used. The tungsten thickness is 2.1mm for the inner 20 layers and 4.2mm for the last 10 layers to reduce the number of readout channels and cost, while maintaining a high sampling rate at the start of the calorimeter. It should be noted that this offers no major gains in terms of energy resolutions in comparison to preexisting particle collider experiments ?? because the focus of this calorimeter is split between imaging the particle showers and recording their energy as opposed to purely focusing on the energy measurement. The 5 mm cell size for the ECal was chosen as a balance between being able to resolve nearby particle showers as well as reducing the overall cost of the calorimeter, which scales with the number of readout channels needed. An optimisation study of the various ECal parameters for the ILD detector can be found in section ??.

As well as including the silicon tungsten sampling calorimeter, the simulation of the ILD ECal contains additional material to represent the instrumented region of the sensor and a heat shield as shown in figure 1.5.



Material	$\lambda_I$ (cm)	$X_0$ (cm)	$\rho_M$ (cm)	$\frac{\lambda_I}{X_0}$
Fe	16.8	1.76	1.69	9.5
Cu	15.1	1.43	1.52	10.6
W	9.6	0.35	0.93	27.4
Pb	17.1	0.56	1.00	30.5

**Table 1.2:** Comparison of the nuclear interaction length  $\lambda_I$ , radiation length  $X_0$  and Molière radius for iron, copper, tungsten and lead. Table taken from [6].

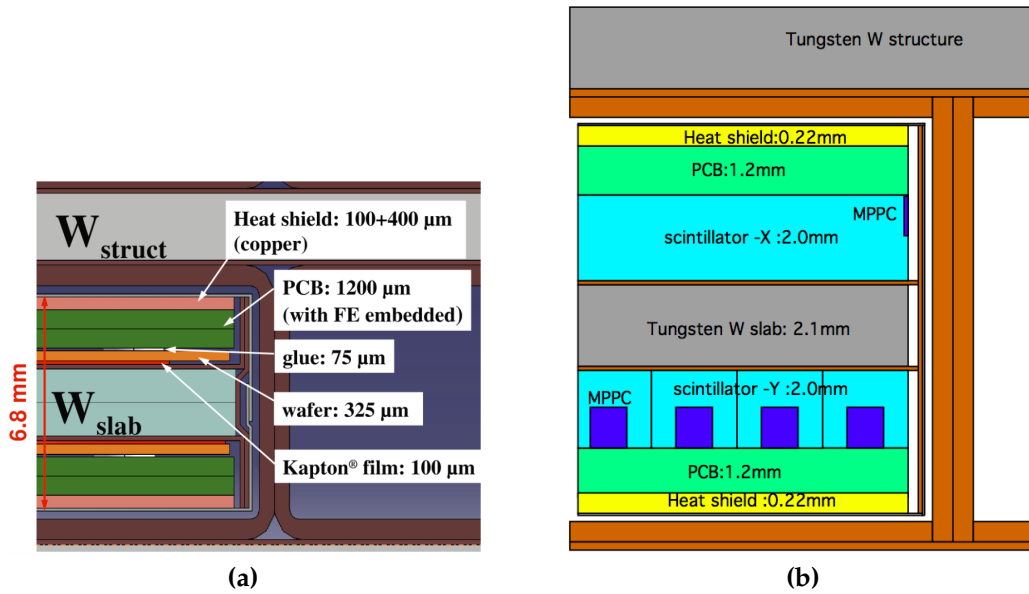


**Figure 1.5:** Cross section through ECal layer for (a) silicon and (b) scintillator option. Figures taken from [2].

### 1.2.3 Hadronic Calorimeter

Surrounding the ECal is a finely segmented hadronic calorimeter (HCal), which has the primary goal of measuring the energy deposits from charged and neutral hadrons. Similarly to the ECal the focus of this HCal is split between being able to resolve nearby particle showers and measuring their energy with a good resolution. The nominal ILD HCal is a scintillator steel sampling calorimeter, which contains 48 layers and uses square cells with side length 30 mm.

Iron is used as the absorber material for the HCal as it has excellent mechanical properties that allow the HCal to be constructed without auxiliary supports, which if required would act as dead regions in the detector. Furthermore, iron is relatively

inexpensive and given the nuclear interaction length is sufficiently small, it is possible to achieve a compact calorimeter design for low cost. The relatively short radiation length found in iron is useful for fine sampling of the electromagnetic shower core that is found in hadronic showers, which exists due to the decays of  $\pi^0$  and  $\eta$  mesons. This fine sampling leads to good energy resolution for the HCal for these shower components. The nominal ILD HCal contains approximately  $6\lambda_I$ , which when combined with the  $1\lambda_I$  in the ECal is sufficient for containing the majority of hadronic showers at ILC like energies. The 48 layers are identical and are comprised of 20 mm of steel absorber with a 3 mm scintillator active medium. The use of a square cell size of 30 mm is again a balance between reducing the cost of the detector, which is proportional to the number of readout channels and thus wants to lower the cell size, and achieving the required spatial resolution to make particle flow calorimetry possible. Overall, the segmentation of the ILD HCal is able to give excellent spatial and energy resolution that can make particle flow a reality. An optimisation study of the various HCal parameters for the ILD detector can be found in section ??.

Simulation of the ILD HCal has a number of realistic features including detailed modelling of the electronics, detector gaps and the implementation of Birk's law for the scintillator sensitive detector elements.

### 1.2.4 Forward Calorimetry

Three additional sampling calorimeters are envisaged for the linear collider, LumiCal, LHCAL and BeamCal, that will extend the coverage of the detector towards  $4\pi$  and monitor the beam quality. The LumiCal will aim to measure the luminosity with a precision of less than  $10^{-3}$  at 500 GeV using Bhabha scattering,  $e^+e^- \rightarrow e^+e^-(\gamma)$ , as a gauge process [1], while the BeamCal will make a bunch-bunch estimate of the luminosity and assist in the beam tuning. Alongside the LumiCal is the LHCAL, which extends the coverage of the HCal to low polar angle as shown in figure 1.6. The LumiCal covers polar angles between 31 and 77 mrad, while the BeamCal covers the range between 5 and 40 mrad. The presence of beam-induced backgrounds along the beam line means these calorimeters will have to be radiation hard.

As the primary focus of these calorimeters is measuring the  $e^+e^-$  beam, they are all constructed using tungsten absorber material to ensure narrow electromagnetic showers form within them. The LumiCal layer configuration mirrors that of the ECal



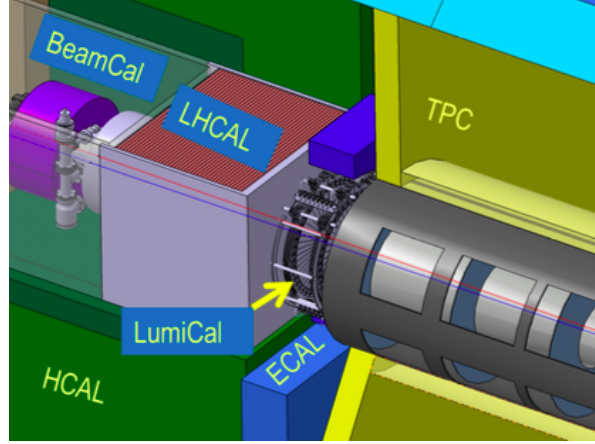


**Figure 1.6:** The very forward region of the ILD detector. LumiCal, BeamCal and LHCAL are carried by the support tube for the final focusing quadrupole, QD0, and the beam pipe. Figure taken from [2].

giving it a total of  $\approx 24X_0$  across its 30 layers. Silicon is used as sensitive detector element for the LumiCal. The LHCAL uses silicon readout sensors identical to those found in the LumiCal and in total the LHCAL contains  $4\lambda_I$  across 40 layers. The BeamCal sensitive detector material is currently being developed as, due to the high occupancy from the beam induced backgrounds, a fast readout is required. The cell sizes for these calorimeters is yet to be confirmed.

In the context of particle flow calorimetry these calorimeters play a minimal role as few particles from the hard physics interaction will have their energy measured in these calorimeters and so they are not used in the reconstruction.

### 1.2.5 Muon Chamber

The ILD outer detector surrounds the HCal and is comprised of a coil, which generates a 3.5 T magnetic field, followed by an iron yoke. The coil is one of the major cost drivers for the ILD detector and to minimise the size it does not encompass the iron yoke. The yoke supplements measurements in the calorimeters by acting as a tail catcher for energy leaking out of the calorimeters and, furthermore, is used in the identification of muons. The yoke is an iron scintillator sampling calorimeter, which consists of 10 layers spaced 14 cm apart followed by 2 (3) layers spaced 60 cm apart for the barrel (endcap) region of the detector as shown in figure 1.7. There is also an additional sensitive layer for the barrel region placed immediately outside the HCal to help with association energy deposits between the calorimeters and the yoke.

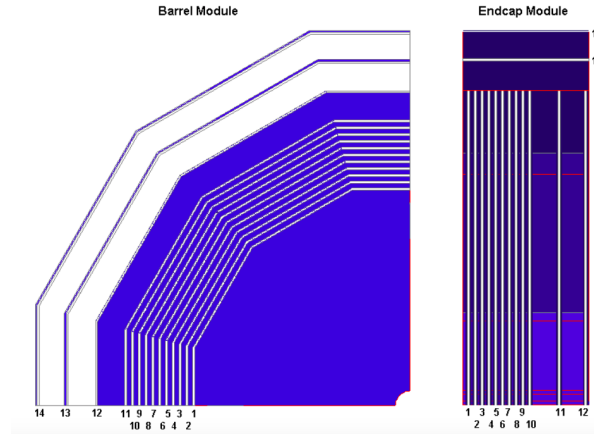


**Figure 1.7:** The sensitive layers of the ILD muon system. Figure taken from [2].

The yoke uses scintillator strip readout technology and in the simulations a square cell size of 30 mm is assumed. This is in contrast to the ILD baseline, which plans to use 3 cm wide and 1 m long strips, however, as the tail-catcher plays a minimal role in particle flow at ILC like energies this difference should have negligible impact.

### 1.2.6 CLIC ILD

It is inappropriate to use the nominal ILD detector for simulations of the CLIC experiment due to the increased collision energy. Therefore, the CLIC experiment has modified the nominal detector model to create a new detector model, CLIC\_ILD [4] shown in figure 1.8, which is more suited to CLIC like conditions. The key differences between the nominal ILD detector and CLIC\_ILD are:

- The higher energies found at the CLIC experiment lead to more intense beam induced backgrounds, which is especially problematic for detectors close to the IP where the occupancies will be extremely high. To attempt to compensate for these effects the inner vertex detector in CLIC\_ILD is moved 15 mm further out from the IP.
- The HCal thickness is increased from  $6 \lambda_I$  to  $7.5 \lambda_I$ . This helps to contain the high energy particle showers found in the CLIC experiment to the calorimeters.
- The HCal absorber material in the barrel is tungsten as opposed to iron. This reduces the overall thickness of the HCal and keeps the coil size, one of the driving cost factors for the detectors, similar for the nominal ILD and CLIC\_ILD

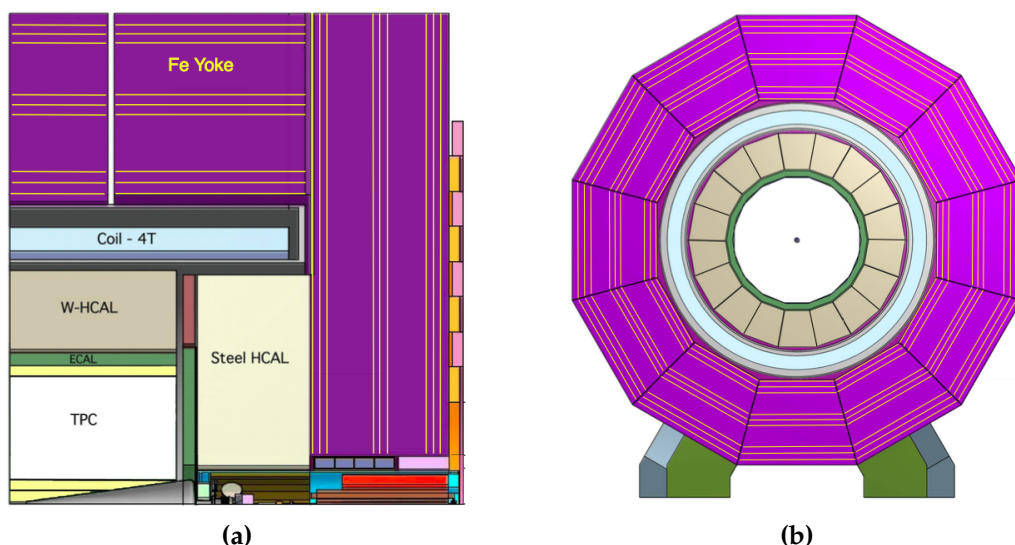


**Figure 1.8:** (a) Longitudinal (top quadrant) and (b) transverse cross section of the CLIC\_ILD detector. Figures taken from [4].

detectors. In the endcaps iron is again used as the absorber material as there are no spatial requirements and it will lower the detector cost. Furthermore, the shower development time in steel is faster than in tungsten making effective time stamping of energy deposits easier, which is crucial for the CLIC experiment for vetoing beam induced backgrounds.

- The magnetic field strength in the CLIC\_ILD detector is increased to 4 T. This was found to benefit the reconstruction, particularly at high energies, as it leads to greater separation of charged particle tracks. Furthermore, it was possible to achieve this increase in field strength using the nominal ILD coil design.

### 1.3 PandoraPFA

Particle flow calorimetry relies upon correct associations being made between calorimetric energy deposits and charged particle tracks. Even with a finely segmented detector, such as the ILD detector described in section 1.2, correctly making these associations is highly a non-trivial task and must be done using advanced pattern recognition software. This is provided by the PandoraPFA particle flow algorithm [5,6].

PandoraPFA applies the pattern recognition logic in eight main stages:

1. Track selection. The input track collections are examined to determine whether  $V^0$  decays, two charged tracks originating from a point displaced from the IP, or kinks, where a charged particle has decayed into a single charged particle and a number of neutral ones, are present. Such information will be propagated in the reconstruction to final PFO creation.
2. Calorimeter hit selection. This stage is broken down into several steps:
  - The various collection of, post digitisation, calorimeter hits are passed into the Pandora framework and converted into Pandora calorimeter hits. These objects are self describing so that the Pandora pattern recognition logic has no dependancy on the external software framework.
  - A minimum ionising particle equivalent energy cut is applied to the calorimeter hits. If a calorimeter hit contains less than 0.5 (0.3) of the energy of a normally incident MIP passing through the ECal (HCal) calorimeter cell is not used in the reconstruction.
  - Calibration of the energy contained within the calorimeter hits is flagged up at this point, however, it is not directly applied at this stage as the energy contribution for each calorimeter cell ultimately depends on whether the associated cluster of calorimeter hits is deemed to originate from an electromagnetic or hadronic showers. Different scale factors are applied to the energy for electromagnetic and hadronic showers to account for effects such as the invisible energy component in hadronic showers. These energy factors are used throughout the reconstruction and for the final reconstructed particle energy once the particle shower type has been identified. For energy comparisons prior to this identification the uncorrected calorimeter hit energy is used. Further details on how these calibration constants are determined can be found in section ??.
  - To minimise any dependancy on the detector geometry each calorimeter hit is assigned to a pseudo-layer, which is representative of the calorimeter stave layer. All further topological association algorithms work using the pseudo-layer definition, illustrated in figure 1.9.
  - If a calorimeter hit is sufficiently far away from other hits, it is flagged as an isolated hit. Such hits are most likely due to low energy neutrons produced in hadronic showers, which can travel a significant distance from the original

shower before depositing energy. These hits are very difficult to associate to the correct cluster of hits and as they do not form the basis of their own shower, they are not used by the initial clustering algorithm.

- Any calorimeter hit that contains an energy consistent with a MIP signal and where, at most, one of the surrounding neighbouring cells in the same layer is above threshold is flagged as a MIP consistent hit. This information is used in the identification of MIPs in the reconstruction.
3. Clustering. This begins by using the projection of the charged particle tracks onto the front face of the ECal as seeds for the initial clustering phase. Calorimeter hits are looped over on a per layer basis, working from the inner to the outer pseudo-layer, and if they fall within a cone of fixed dimensions surrounding a cluster direction they are associated to the cluster. If no association can be made to any preexisting calorimeter hit clusters then the calorimeter hit is used to seed a new cluster.
  4. Topological cluster merging. The initial clustering algorithm is designed to be conservative to avoid mixing together energy deposits from several particles. The fragments produced by the initial clustering are then merged together by various algorithms whose logic is motivated by a number of well-motivated topological rules, such as those shown figure 1.10.
  5. Statistical re-clustering. Comparisons between the cluster energy and any associated track momenta are made to determine whether they are consistent. If a large discrepancy is observed then statistical reclustering is initiated. This involves running a number of differently configured algorithms to change the cluster configuration to determine the optimal configuration of tracks and clusters.
  6. Photon identification and recovery. Topological likelihood data is used to then identify clusters of calorimeter hits that are consistent with  $\gamma$ s. This is possible due to the clear transverse and longitudinal profiles observed for electromagnetic showers.
  7. Fragment removal. This step aims to remove neutral clusters that have been created that actually originate from a nearby charged particle cluster. These algorithms take into account the changes in the compatibility of the track and cluster association when merging any neutral clusters into charged clusters.

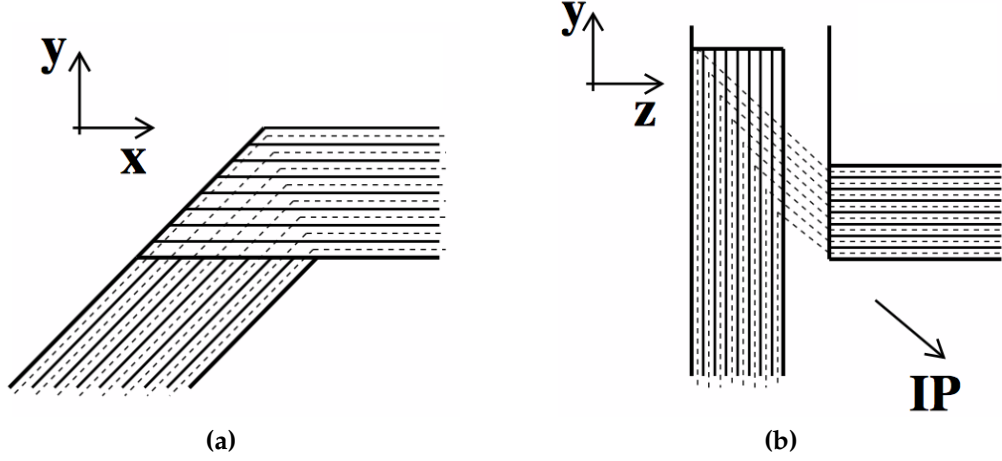


**Figure 1.9:** Schematic showing the definition of the pseudo-layer assignment for calorimeter hits. The solid lines indicate the positions of the physics ECal layers and the dashed lines show the definition of the virtual pseudo-layers. (a) The  $xy$ -view showing the ILD ECal stave structure. (b) The  $xz$  view showing a possible layout for the ECal barrel/endcap overlap region. The pseudo-layers are defined using projection back to the IP. Figures taken from [6].

8. Formation of particle flow objects. Finally, reconstructed particles are produced. The energy for charged particles is taken from the track momenta while neutral particle energies are taken from the calorimeter cluster measurements. Furthermore, the different electromagnetic and hadronic scales are applied to the output neutral particle energies depending on whether the neutral cluster is consistent with a  $\gamma$ .

The application of the pattern recognition algorithms in PandoraPFA when combined with a highly segmented detector, such as the ILD detector, make particle flow calorimetry a reality, which in turn provides excellent jet energy resolution for studying many interesting physics processes at the future linear collider.

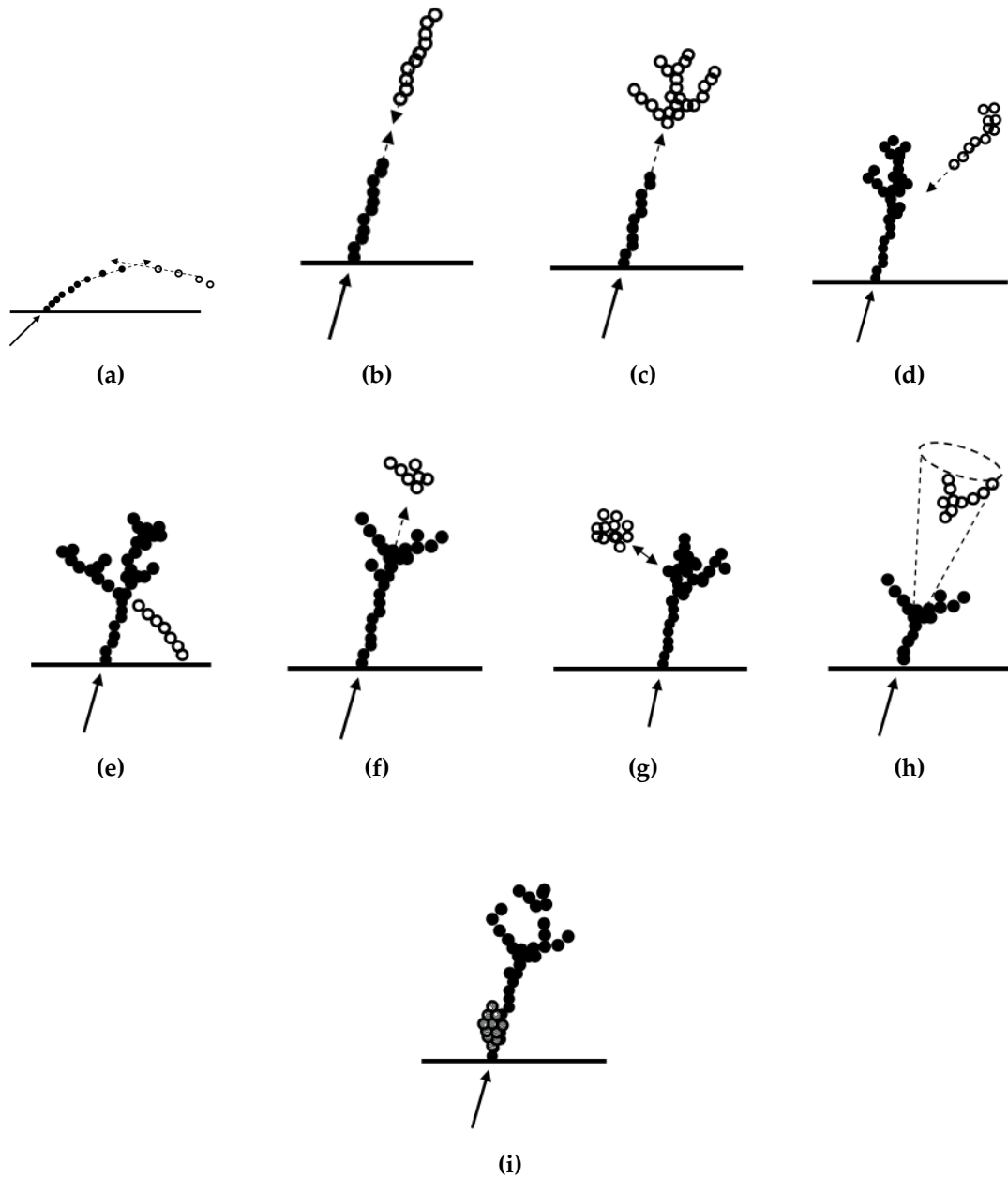


**Figure 1.10:** The main topological rules for cluster merging: (a) looping track segments; (b) track segments with gaps; (c) track segments pointing to hadronic showers; (d) track-like neutral clusters pointing back to a hadronic shower; (e) back-scattered tracks from hadronic showers; (f) neutral clusters which are close to a charged cluster; (g) a neutral cluster near a charged cluster; (h) cone association; and (i) recover of photons which overlap with a track segment. In each case the arrow indicates the track, the filled points represent the hits in the associated cluster and the open points represent hits in the neutral cluster. Figures taken from [6].





# Colophon

This thesis was made in  $\text{\LaTeX}2_\epsilon$  using the “hepthesis” class [3].



# Bibliography

- [1] Toshinori Abe et al. The International Large Detector: Letter of Intent. 2010, 1006.3396.
- [2] Halina Abramowicz et al. The International Linear Collider Technical Design Report - Volume 4: Detectors. 2013, 1306.6329.
- [3] Andy Buckley. The hepthesis L<sup>A</sup>T<sub>E</sub>X class.
- [4] Lucie Linssen, Akiya Miyamoto, Marcel Stanitzki, and Harry Weerts. Physics and Detectors at CLIC: CLIC Conceptual Design Report. 2012, 1202.5940.
- [5] J. S. Marshall, A. M<sup>Ä</sup>ijnnich, and M. A. Thomson. Performance of Particle Flow Calorimetry at CLIC. *Nucl. Instrum. Meth.*, A700:153–162, 2013, 1209.4039.
- [6] M. A. Thomson. Particle Flow Calorimetry and the PandoraPFA Algorithm. *Nucl. Instrum. Meth.*, A611:25–40, 2009, 0907.3577.



# List of figures

1.1	A typical simulated 250 GeV jet in the CLIC_ILD detector, with labels identifying constituent particles. Image taken from [5]. . . . .	3
1.2	(a) Quadrant view of the ILD detector concept. The interaction point is in the lower right corner of the picture. Dimensions are in mm. (b) View of the ILD detector concept. Figures taken from [2]. . . . .	4
1.3	(a) A quadrant view of the ILD silicon envelope made of the four components SIT, SET, ETD and FTD as included in the full MOKKA simulation. (b) a 3D detailed GEANT4 simulation description of the silicon system. Figures taken from [2]. . . . .	6
1.4	(a) Drawing of the propose end-plate for the TPC. (b) Conceptual sketch of the TPC system showing the main parts of the TPC (not to scale). Figures taken from [2]. . . . .	7
1.5	Cross section through ECal layer for (a) silicon and (b) scintillator option. Figures taken from [2]. . . . .	9
1.6	The very forward revion of the ILD detector. LumiCal, BeamCal and LHCAL are carried by the support tube for the final focusing quadrupole, QD0, and the beam pipe. Figure taken from [2]. . . . .	11
1.7	The sensitive layers of the ILD muon system. Figure taken from [2]. . .	12
1.8	(a) Longitudinal (top quadrant) and (b) transverse cross section of the CLIC_ILD detector. Figures taken from [4]. . . . .	13

- 1.9 Schematic showing the definition of the pseudo-layer assignment for calorimeter hits. The solid lines indicate the positions of the physics ECal layers and the dashed lines show the definition of the virtual pseudo-layers. (a) The  $xy$ -view showing the ILD ECal stave structure. (b) The  $xz$  view showing a possible layout for the ECal barrel/endcap overlap region. The pseudo-layers are defined using projection back to the IP. Figures taken from [6]. . . . . 16
- 1.10 The main topological rules for cluster merging: (a) looping track segments; (b) track segments with gaps; (c) track segments pointing to hadronic showers; (d) track-like neutral clusters pointing back to a hadronic shower; (e) back-scattered tracks from hadronic showers; (f) neutral clusters which are close to a charged cluster; (g) a neutral cluster near a charged cluster; (h) cone association; and (i) recover of photons which overlap with a track segment. In each case the arrow indicates the track, the filled points represent the hits in the associated cluster and the open points represent hits in the neutral cluster. Figures taken from [6]. . . . . 17

# List of tables

1.1	The approximate jet fractions and energy resolutions for charged particles ( $X^\pm$ ), photons ( $\gamma$ ) and neutral hadrons ( $X^0$ ). Taken from [6]. . . .	2
1.2	Comparison of the nuclear interaction length $\lambda_I$ , radiation length $X_0$ and Molière radius for iron, copper, tungsten and lead. Table taken from [6]. . . . .	9